Article

Loss induced delocalization of topological boundary modes

Yugan Tang[1,7], Jien Wu[2,7], Pengtao Lai[1], Yejian Hu[3], Hui Liu[1], Weiyin Deng [3] ✉, Hua Cheng [1] ✉, Zhengyou Liu [3,4] ✉ & Shuqi Chen [1,5,6] ✉

The introduction of non-Hermiticity has inspired abundant intriguing phenomena to topological physics. As a significant part of non-Hermiticity, losses are generally inevitable, represent a natural tendency of open systems, and can be readily regulated by straightforward passive components. However, losses are originally considered obstructive to topological systems and usually enable the localization of states. Here, we present that reciprocal loss can induce delocalization of topological boundary modes, which is essentially distinct from non-reciprocal mechanisms. By precisely regulated imaginary hopping via loss, the end modes in one dimension and the corner modes in two and three dimensions of topological insulators are delocalized to the bulk, accompanied by the non-Hermitian skin effects. Our theory is implemented in passive electric circuits with resistance as non-Hermitian loss, and the topological delocalized modes are well visualized experimentally. The realized topological delocalized modes are still robust against disorders and possess a broadband property. Our work establishes an important missing link between topology and loss, and brings a unique vision for compact topological applications.

Topological materials, a subject of intense research, are mainly known for their topological boundary modes (TBMs), where the bulk properties give rise to these unique modes exponentially localized at ends, boundaries or defects of lattice[1–3]. These TBMs are characterized by their robustness against local disorders or immunity to backscattering, thereby exploring widely in condensed matters, photonic, acoustic, and electric circuit systems[4–14]. With the presence of non-Hermitian interaction of gain, loss or non-reciprocity, the system usually hosts the complex spectrum, enabling innovative mechanisms to manipulate TBMs[15–30]. For example, the gain medium can perform the TBMs to generate amplified topological whispering gallery modes as a sound laser[30]. The non-reciprocal hoppings generally can give rise to the non-Hermitian skin effect (NHSE)[20–28,31–34], which causes the eigenstates of

open lattice to exponentially collapse toward its boundaries, making the TBMs further localized[20,21] or even delocalized[22–28]. Such topological delocalized modes (TDMs) remain topologically nontrivial and exhibit the same robustness as localized TBMs, enabling topological applications based on all sites regardless the bulk of lattice. However, the non-reciprocal hoppings enabled by active devices easily render the system complicated and unstable, thereby hindering device miniaturization and the advancement of high-dimensional systems.

As an important component of non-Hermiticity, loss mirrors the inevitable trend of open systems, which is originally thought of harmful and limited due to energy dissipation. However, recent studies discover that loss can play an important role in topological physics, which facilitate the re-formulation of Bloch band theory and

topological descriptions in non-Hermitian systems. On the one hand, by employing the deliberately introduced loss, the trivial topological phases can be transformed into nontrivial ones with TBMs, such as end mode[35,36] and corner mode[37]. On the other hand, the loss can contribute systems to form nonzero spectral winding numbers, resulting in NHSEs[38-43], including the geometry-dependent skin effect for the bulk modes[40-42] and hybrid skin-topological effects for the TBMs[43]. Distinguished from complicated gain and non-reciprocal interactions, the loss modulation necessitates only passive and simple structures that afford greater flexibility and maintain system stability independent of dimensions, site numbers and non-Hermitian hopping strengths. It obviously promotes the development of high-dimensional topological physics and is applicable across diverse fields. Nevertheless, loss is inherently reciprocal and is generally considered leading to the localization of states in previous understanding. Considering the state propagation, loss naturally induces state decay in space and be localized. In the context of steady state, previous studies widely accept that loss can induce generalized reciprocal skin effects and localize eigenstates at boundaries[39-43]. A counterintuitive question is that whether the reciprocal loss can be harnessed to delocalize the originally localized TBMs.

Here, we provide the reciprocal solution and demonstrate the delocalization of TBMs in non-Hermitian topological insulators with hopping loss. Our design is based on the bilayer strategy with pseudospin degree of freedom, and the loss plays the role to spin polarized non-reciprocal imaginary hoppings. They can achieve the NHSEs whose accumulated directions are locked to spins. Through the precisely regulated parameter of loss, the in-gap TBM can be delocalized into bulk and form a spin polarized TDM. Such TDM is still nontrivial protected by a nonzero topological invariant. Meanwhile, the TDM originates from spin-dependent wavefunction topology, while its delocalization direction aligns with the spin polarized skin effect that relates to spin-dependent spectral topology. It is fundamentally distinguished from previous non-reciprocal studies that rely on spinless wavefunction and spectral topologies[22-28]. We first introduce the lattice model with topological end modes in one-dimensional (1D) topological insulator. The spin polarized TDM and complex spectra are visualized in 1D passive electric circuit with resistances in experiments. Then, we extended the study to two-dimensional (2D) and three-dimensional (3D) lattice models, where the TDMs delocalized from topological corner modes (TCMs) are well observed in 2D and 3D passive electric circuits. The solid results in 1D, 2D and 3D all demonstrate that the reciprocal theory of loss utilization and the passive experimental method bring significant insights into non-Hermitian physics.

Results
Loss induced delocalization of topological end mode in 1D
We commence by a tight-binding model on a duplex non-Hermitian chain, pictorially shown in the top panel of Fig. 1a, which is stacked by two identical Su-Schrieffer-Heeger (SSH) single chains employing interlayer hoppings. Each unit cell consists of four sites 1–4, the intracell hopping is pure imaginary with $i\gamma$, where γ represents the amplitude of designed loss; the intercell hopping is t_1 and $\pm t_0$ indicate the positive and negative interlayer hoppings, respectively. On the basis of sites 1–4, the non-Hermitian Hamiltonian in momentum space can be expressed as

$$H_1(k) = (t_1 \cos k + i\gamma)\tau_x\sigma_0 + t_1 \sin k\tau_y\sigma_0 + t_0\tau_y\sigma_y, \tag{1}$$

where k represents the wavevector, $\boldsymbol{\tau}$ and $\boldsymbol{\sigma}$ denote the Pauli matrices for sublattice and layer degrees of freedom, respectively. It can be separated into two independent blocks via the unitary transformation

$$H_1'(k) = T_1 H_1(k) T_1^{-1} \quad \text{with} \quad T_1 = \frac{1}{\sqrt{2}}\tau_0 \begin{pmatrix} 1 & i \\ 1 & -i \end{pmatrix}, \quad \text{denoted as}$$

$H_1' = \begin{pmatrix} H_{1\uparrow} & 0 \\ 0 & H_{1\downarrow} \end{pmatrix}$, where $H_{1\uparrow(\downarrow)} = (t_1 \cos k + i\gamma)\tau_x + (t_1 \sin k + (-)t_0)\tau_y$. As shown in the bottom panel of Fig. 1a, the two blocks are named spin up and spin down respectively. As a result, through the designed loss regulated by γ, the spin-dependent non-reciprocal imaginary hoppings are obviously constructed with $i(\gamma \pm t_0)$ for spin up and $i(\gamma \mp t_0)$ for spin down. Notably, the underlying physics of the bilayer model is essentially distinct from that in previous non-reciprocal studies. The entire system is inherently reciprocal and obeys spinful anomalous time-reversal symmetry, $U_T H^T(k) U_T^{-1} = H(-k)$ with $U_T^2 = -1$, which fundamentally differs from the non-reciprocal systems that maintain time-reversal symmetry, $U_T H^*(k) U_T^{-1} = H(-k)$ with $U_T^2 = 1$.

In the presence of loss, the open boundary condition (OBC) and periodic boundary condition (PBC) spectra are calculated in the top panel of Fig. 1b, which do not coincide with each other. In particular, the band closure points ($|E| = 0$) of them are inconsistent, indicating the broken bulk-boundary correspondence. To better describe the topological properties of the spectrum, the Hamiltonian of either spin can be written in the form of $H(\beta) = \begin{pmatrix} 0 & H_{ab}(\beta) \\ H_{ba}(\beta) & 0 \end{pmatrix}$, where β is the Bloch phase factor $\beta = e^{ik}$. Under PBC, β_{BZ} is a unit circle on the complex plane, forming the Brillouin zone (BZ). Under OBC, since the introduction of loss, k is a complex value, and the trajectory formed by β_{GBZ} does not coincide with BZ, forming the generalized Brillouin zone (GBZ). Based on the GBZ, we employ the non-Bloch winding number W_{GBZ} to describe the topological properties of the OBC spectrum, where $W_{GBZ} = \frac{1}{2\pi}\oint_{GBZ} \arg\frac{H_{ab}(\beta_{GBZ})}{H_{ba}(\beta_{GBZ})} d\beta_{GBZ}$ (Supplementary Section 1). As shown in the bottom of Fig. 1b, the topological phase transition points are at $\gamma = \pm\sqrt{t_1^2 + t_0^2}$, which are the same with the closure points of OBC spectrum. The spectra and topological invariants are the same for two spins. Hence, by setting $|\gamma| < \sqrt{t_1^2 + t_0^2}$, we can get a pair of spin polarized topological end modes at $|E| = 0$, which are not affected by the closure of the PBC spectra.

The Bloch winding number W_{BZ} defined in BZ is employed to describe the localization property of end mode, as shown in the bottom of Fig. 1b, where $W_{BZ} = \frac{1}{2\pi}\oint_{BZ} \arg\frac{H_{ab}(\beta_{BZ})}{H_{ba}(\beta_{BZ})} d\beta_{BZ}$ (Supplementary Section 1). It is also the same for two spins. When the Bloch winding number changes, one end mode is expected to reverse its localization direction and localize at the opposite end[26,44,45]. Therefore, at the transition point $\gamma_c = -t_0 \pm |t_1|$, the end mode is naturally delocalized as a TDM. In this time, the PBC spectrum closes and coincides with the end mode of OBC spectrum under chiral symmetry, forming the Bloch points[46,47], as shown in Fig. 1c.

Although the spectra for two spins are identical on the complex plane, the PBC spectral winding directions are opposite, caused by the introduced loss and arising from spin-dependent spectral topology. This indicates the appearance of spin polarized NHSEs (left-localized and right-localized skin effects for spin up and spin down, respectively), which essentially represent the generalized reciprocal skin effects with zero current functionals (as shown in Fig. S1 of Supplementary Section 1). Accordingly, the delocalization directions of end modes align with the spin polarized skin NHSEs. For instance, when $\gamma = \gamma_c$, the right end mode for spin up and the left end mode for spin down are simultaneously delocalized in the left and right directions, respectively. To simplify the discussion, we cut off two sites at right end of the duplex chain and leave only end modes at left for two spins (Supplementary Section 2). In addition, the Bloch winding number cannot predict the appearance or disappearance of end mode in OBC. The nontrivial topological property of end mode should still be described by the non-Bloch winding number, while the critical
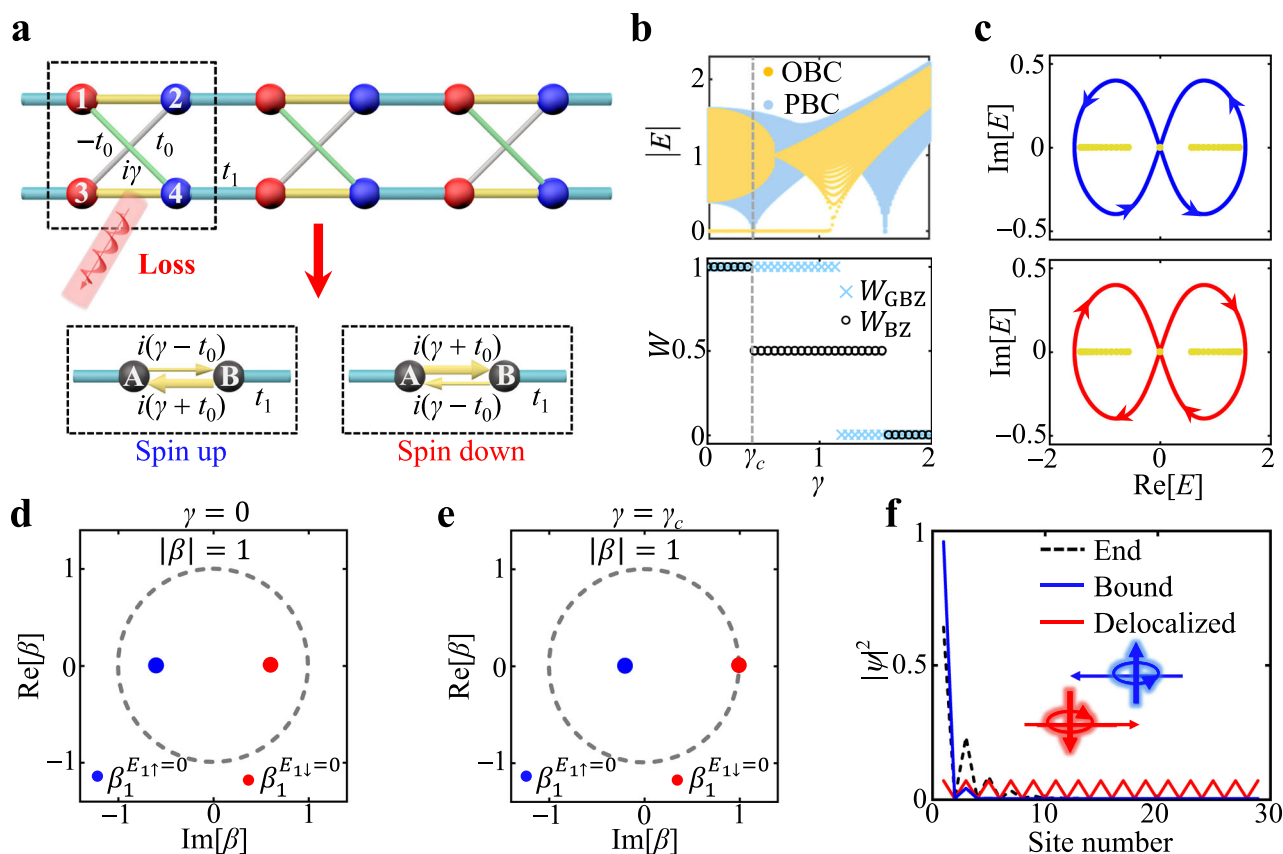
Fig. 1 | Loss induced delocalization of topological end mode in 1D. a Schematic of a duplex non-Hermitian SSH lattice. The black dashed box encloses a unit cell, which can be decoupled into two spin models. The red and blue balls conceptually indicate the corresponding sublattices. The yellow and light blue sticks are intracell and intercell hoppings, respectively, where the red vortex represents loss. The gray and green sticks represent the positive and negative hoppings, respectively. The black balls located below represent the sublattices of spin models. **b** Spectra of OBC and PBC as a function of γ with $t_0 = 0.6$, $t_1 = -1$ and $\gamma_c = 0.4$. The gray dashed line denotes the position of Bloch point. The topological phase diagrams are displayed

in the bottom. The topological end modes (yellow points at $|E| = 0$) appear when $|\gamma| < \sqrt{t_1^2 + t_0^2}$. **c** Complex spectra of OBC and PBC for two spins at $\gamma = \gamma_c$. The zero energy of OBC intersects with PBC spectrum forming Bloch point. The arrows indicate the winding directions of spectral loops. **d, e** Relations between BZ and Bloch phase factors of left end modes for two spins at $\gamma = 0$ and $\gamma = \gamma_c$, respectively. **f** Wavefunction intensities of the end modes at $\gamma = \gamma_c$. The topological end modes are fully delocalized for spin down and more localized for spin up. The OBC chain possesses 58 sites after cut off the right two sites.

parameter γ_c has no influence on it. Consequently, the loss induced TDM is always nontrivial yet delocalized rather than localized, characterizable by both Bloch and non-Bloch winding numbers, analogous to the winding tuple[48].

To intuitively illustrate the loss induced TDM, we employ the GBZ approach by calculating the Bloch phase factor. In fact, a point in the GBZ corresponds to an OBC eigenstate, whose wavefunction at l-th sublattice site satisfies $\psi_l \propto \beta_{GBZ}^l$ [36]. For the Bloch point, owing to the same eigenvalues of PBC and OBC spectra, there is $\beta_{GBZ} = \beta_{BZ}$, i.e., $|\beta_{GBZ}| = 1$, giving rise to the delocalized mode for its eigenstate. The Bloch phase factors of the left end modes for spin up and spin down can be derived as $\beta_1^{E_{1\uparrow} = 0} = -i\frac{\gamma - t_0}{t_1}$ and $\beta_1^{E_{1\downarrow} = 0} = -i\frac{\gamma + t_0}{t_1}$ at $E = 0$, respectively, which represent the wavefunction decay ratios of end modes (Supplementary Section 1). Their wavefunctions at l-th sites A thus obey $A_{l,\uparrow} \propto (\beta_1^{E_{1\uparrow} = 0})^l$ and $A_{l,\downarrow} \propto (\beta_1^{E_{1\downarrow} = 0})^l$, while that at sites B are zero as $B_l = 0$. As observed, the loss can change the decay ratios of the end mode via the spin-dependent non-reciprocal imaginary hoppings, thereby counteracting the localization.

When $\gamma = 0$, both $\left|\beta_1^{E_{1\uparrow} = 0}\right| < 1$ and $\left|\beta_1^{E_{1\downarrow} = 0}\right| < 1$ holding within the BZ indicate that the end modes are localized at left ends, as shown in Fig. 1d. When $\gamma = \gamma_c$, $\left|\beta_1^{E_{1\downarrow} = 0}\right| = 1$ intersects with BZ and forms Bloch point in spectra, resulting a TDM rather than a localized mode for spin down, as shown in Fig. 1e. In this time, the Bloch winding number is changed (Supplementary Section 1). Meanwhile, the left end mode for

spin up becomes more localized with $\left|\beta_1^{E_{1\uparrow} = 0}\right| < 1$. Therefore, when taking $\gamma = \gamma_c$, the excellent TDM for spin down occupying the entire chain and the bound mode for spin up being more localized are plotted in Fig. 1f, which are reshaped from the topological end modes. The reciprocal bilayer model, combining pseudospin degree of freedom with loss, consequently determines the formation of spin polarized TDM, where the designed loss is mainly responsible for the delocalization of topological end modes. It is fundamentally distinct from previous works (Supplementary Section 3).

In order to experimentally realize the loss induced delocalization of TBMs, we introduce a 1D passive electric circuit that based on the duplex non-Hermitian chain, as depicted in Fig. 2a. The electric circuit systems are widely accepted as the critical platform for research and experimental demonstration of non-Hermitian topological physics[49–55]. In matrix form of Kirchhoff's law, the response of a circuit system is described by $I = JV$, where I and V denote the input current and voltage at all nodes, and J is the circuit Laplacian or admittance matrix similar to the Hamiltonian of system. Naturally, the eigenvalues j and eigenstates ϕ of Laplacian J take the similar roles to the eigenvalues and eigenstates of Hamiltonian. Supplementary Section 4 recapitulates how our Laplacian relates to the tight-binding model. For our 1D electric circuit with a given frequency $\omega = 2\pi f$, the Laplacian can be written as $J_1(k) = i\omega [H_1(k) + E_1]$, where E_1 represents the diagonal matrix. Obviously, the real and imaginary parts of the Laplacian's
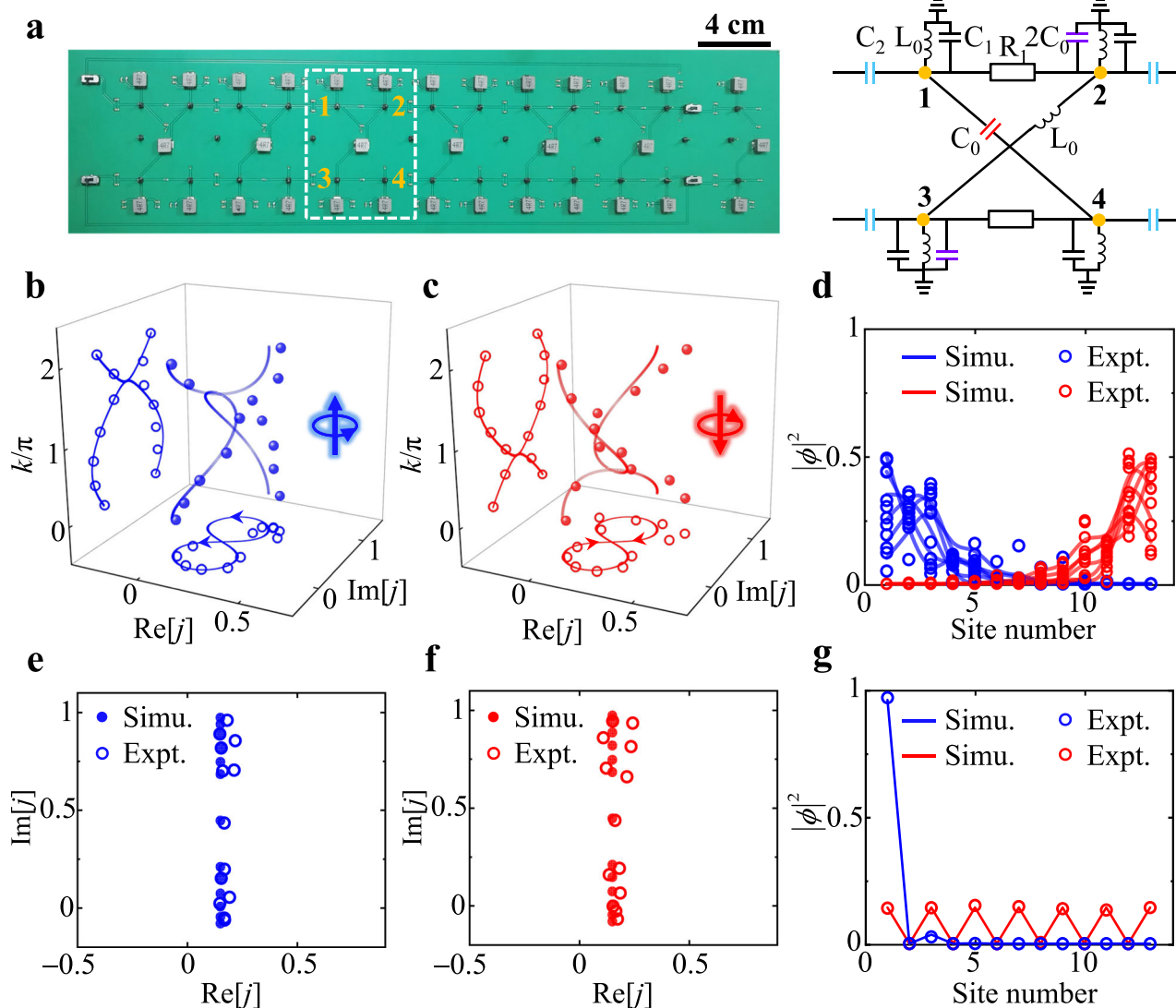
Fig. 2 | Observation of the loss induced delocalization effect in 1D. a Photograph of the 1D circuit sample. The dashed box indicates a circuit unit cell, whose design diagram is schematically shown on the right. The nodes 1–4 are correspond to the sublattices in 1D non-Hermitian lattice. The resistance R_1 and capacitance C_2 represent the intracell and intercell hoppings, respectively. The positive and negative interlayer hoppings are constructed through the inductance L_0 and capacitance C_0, respectively. Each node is grounded through a certain inductance and capacitance. **b, c** Measured PBC spectra for spin up and spin down, respectively. The lines represent results in theory. The balls and unfilled circles represent the measured eigenvalues in the 3D parameter space and their projections in the 2D parameter space, respectively. **d** Measured and simulated wavefunction intensities of all the bulk eigenstates for two spins, showing the spin polarized NHSEs. **e, f** OBC spectra for spin up and spin down, respectively. **g** Corresponding intensity distributions of the end modes, confirming the TDM for spin down.

eigenvalues are inversely related to the counterparts of the Hamiltonian. The circuit unit cell corresponding to the one of lattice model is detailed shown in the right side of Fig. 2a, where the imaginary intracell hopping is indicated by the resistance R_1 with $i\gamma \rightarrow \frac{i}{\omega R_1}$, which still represents loss in circuit; the positive and negative interlayer hoppings are constructed through the inductance L_0 with $t_0 \rightarrow \frac{1}{\omega^2 L_0}$ and capacitance C_0 with $-t_0 \rightarrow -C_0$, respectively, which requires $f = \frac{1}{2\pi\sqrt{L_0 C_0}}$ as the critical frequency f_0 to make sure this; the intercell one is C_2 with $t_1 \rightarrow -C_2$. In addition, C_1 is capacitance to act on E_0. In the same way, the Laplacian can also be decoupled into two spin parts, which still possesses spin polarized topological end modes. To form the TDM for spin down, it is needed $R_1 = \frac{2\pi}{f_0(-C_0 \mp C_2)}$ to satisfy $\gamma = \gamma_c$.

Hence, by taking the resistance with loss, we can similarly delocalize the end mode of the Laplacian for spin down. With successfully obtaining the imaginary part, the PBC spectra of two spins are independently measured, as shown in Fig. 2b, c, respectively,

which form the complex loops. While the opposite winding directions along the momentum k have also been observed, these results clearly indicate spin polarized NHSEs originating from spin-dependent spectral topology. The measured OBC bulk eigenstates of Laplacian shown in Fig. 2d demonstrate them with left and right skin directions. The measured OBC spectra for two spins are shown in Fig. 2e, f, respectively, which exhibit the end modes are still in the gap. The end mode of spin down is finally delocalized via loss, forming a flat TDM, as shown by the red points and line in Fig. 2g, while the bound mode of spin up is simultaneously obtained at operated frequency $f = 178$ kHz.

Second-order delocalization of TCM via loss in 2D
Furthermore, we demonstrate the ability of loss can be extended to high-dimensional topological systems. A rhombic geometry of bilayer kagome lattice in 2D is introduced and schematically shown in Fig. 3a. A unit cell contains three sites 1–3 in each layer, and the intracell hopping is zero between sites 2 and 3, while the hoppings in
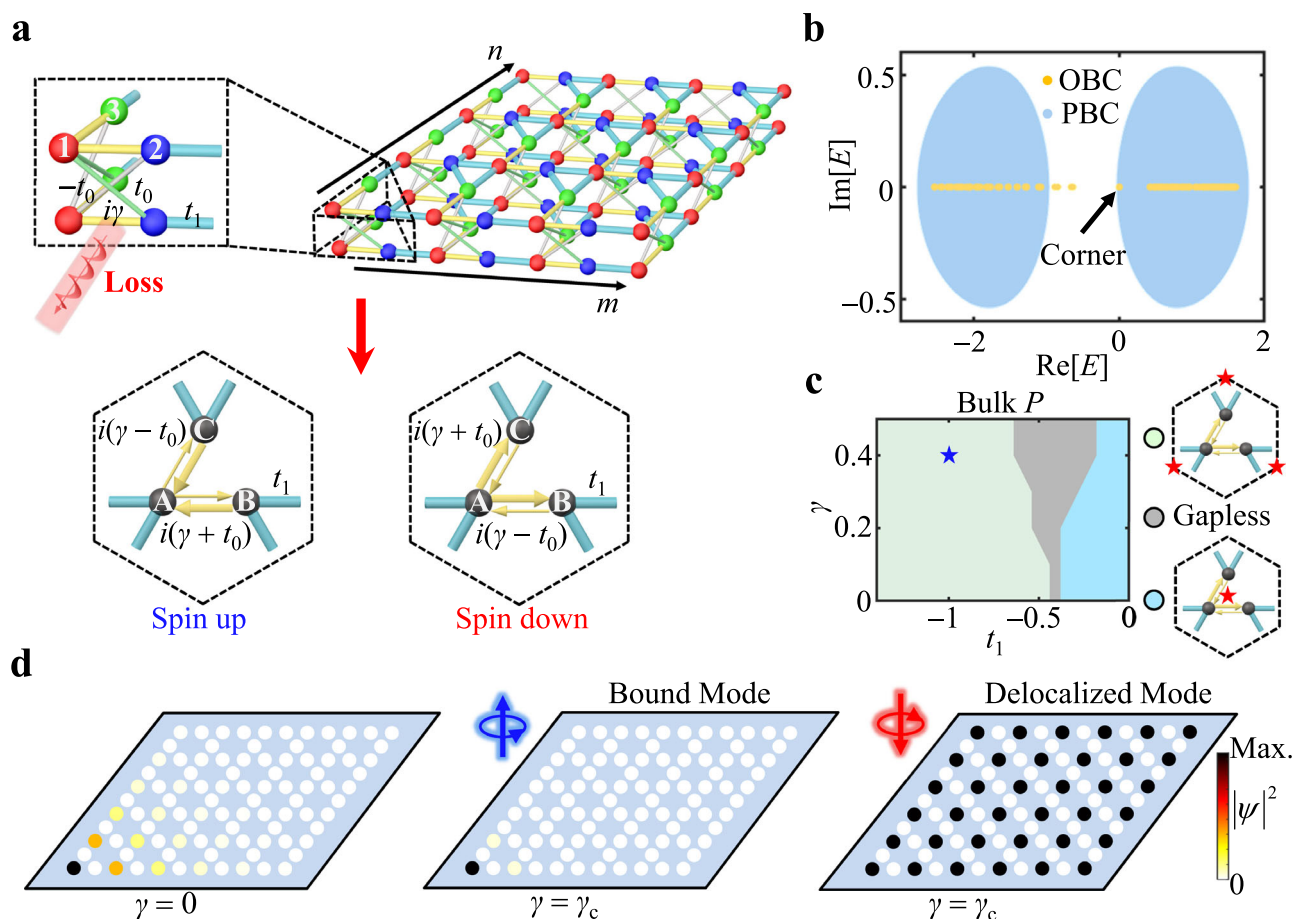
Fig. 3 | Second-order delocalization of TCM via loss in 2D. a Conceptual illustration of the bilayer kagome lattice. The red, blue and green balls represent different sublattices of theoretical model. The sticks with different colors are the same with 1D case, which represent different hoppings. The unit cell encircled by the black dashed box can be separated into a pair of spin-polarized models. The colors in the spin models are also the same with those in 1D. **b** PBC and OBC spectra, where the rhombic sample has 192 sites. **c** Topological phase diagram of spin down model with $t_0 = 0.6$. It is also the same for spin up. The green, gray and blue colors indicate the nontrivial phase, gapless and trivial phase, respectively. The blue star marks the parameters of TDM. The red stars conceptually indicate the location of Wannier centers. **d** Wavefunction intensities of TCMs at different parameters for spin up and spin down, respectively. The parameters are chosen as $t_0 = 0.6$, $t_1 = -1$ with $\gamma_c = 0.4$.

m and n directions are the same with the above 1D chain. Hence, the Hamiltonian $H_2(\boldsymbol{k})$ can also be separated into two independent blocks with $H'_2 = \begin{pmatrix} H_{2\uparrow} & 0 \\ 0 & H_{2\downarrow} \end{pmatrix}$, as shown in the bottom of Fig. 3a (Supplementary Section 5). Notably, the equivalent non-reciprocal imaginary hoppings of each spin are constructed in m and n directions via the deliberately introduced loss. For spin down case, the Hamiltonian can be written as

$$H_{2\downarrow} = \begin{pmatrix} 0 & i(\gamma - t_0) + h_{12} & i(\gamma - t_0) + h_{13} \\ i(\gamma + t_0) + h_{12}^* & 0 & h_{23} \\ i(\gamma + t_0) + h_{13}^* & h_{23}^* & 0 \end{pmatrix}, \quad (2)$$

where $h_{12} = t_1 e^{-ik_x}$, $h_{13} = t_1 e^{-i(k_x + \sqrt{3}k_y)/2}$ and $h_{23} = t_1 e^{-i(-k_x + \sqrt{3}k_y)/2}$. The PBC and OBC spectra are shown in Fig. 3b. In this case, the spectrum of PBC has nonzero spectral area in the complex plane. And more importantly, a second-order TCM emerges in OBC spectrum, which can be similarly delocalized to form a TDM via loss. To demonstrate it, the wavefunction decay ratios of TCM are calculated by solving the OBC real-space eigen-equations, which are expressed as

$$E_{2\downarrow} C_{\downarrow,(i,g)} = t_1 A_{\downarrow,(i,g+1)} + i(\gamma + t_0) A_{\downarrow,(i,g)} + t_1 B_{\downarrow,(i-1,g+1)},$$

$$E_{2\downarrow} B_{\downarrow,(i,g)} = t_1 A_{\downarrow,(i+1,g)} + i(\gamma + t_0) A_{\downarrow,(i,g)} + t_1 C_{\downarrow,(i+1,g-1)}, \quad (3)$$

where $A_{\downarrow,(i,g)}$, $B_{\downarrow,(i,g)}$ and $C_{\downarrow,(i,g)}$ represent the wavefunction components on the i-th and g-th sublattice sites in m and n directions, respectively. Since the wavefunction of TCM has nonzero components only at sites A with a zero energy of $E_{2\downarrow} = 0$, the wavefunction decay ratios at sites A are obtained as $\epsilon_{A,\downarrow,n} = \frac{A_{\downarrow,(i,g+1)}}{A_{\downarrow,(i,g)}} = -i\frac{\gamma + t_0}{t_1}$ in n direction and $\epsilon_{A,\downarrow,m} = \frac{A_{\downarrow,(i+1,g)}}{A_{\downarrow,(i,g)}} = -i\frac{\gamma + t_0}{t_1}$ in m direction. The parameter $\gamma = \gamma_c$ leads to $|\epsilon_{A,\downarrow,n}| = |\epsilon_{A,\downarrow,m}| = 1$, resulting in a second-order delocalization of the TCM for forming a fully delocalized mode in the entire 2D spin down lattice. The TDM here is still topologically nontrivial, which is demonstrated by employing the non-Hermitian bulk polarization[56] and shown in Fig. 3c (Supplementary Section 5). Notably, non-Hermitian bulk polarization is accurate when the non-Hermitian intensity is not strong. The nontrivial phase, colored green, exhibits Wannier centers positioned at the centers of downward-pointing triangles, marked by red stars in Fig. 3c. In the trivial phase, represented by blue color, the Wannier centers are located at the centers of upward-pointing triangles. The bulk polarization cannot be calculated when the PBC spectrum is closed, which is represented by gapless (gray color). Compared with the originally localized TCM, the bound mode and TDM have been clearly depicted in Fig. 3d.
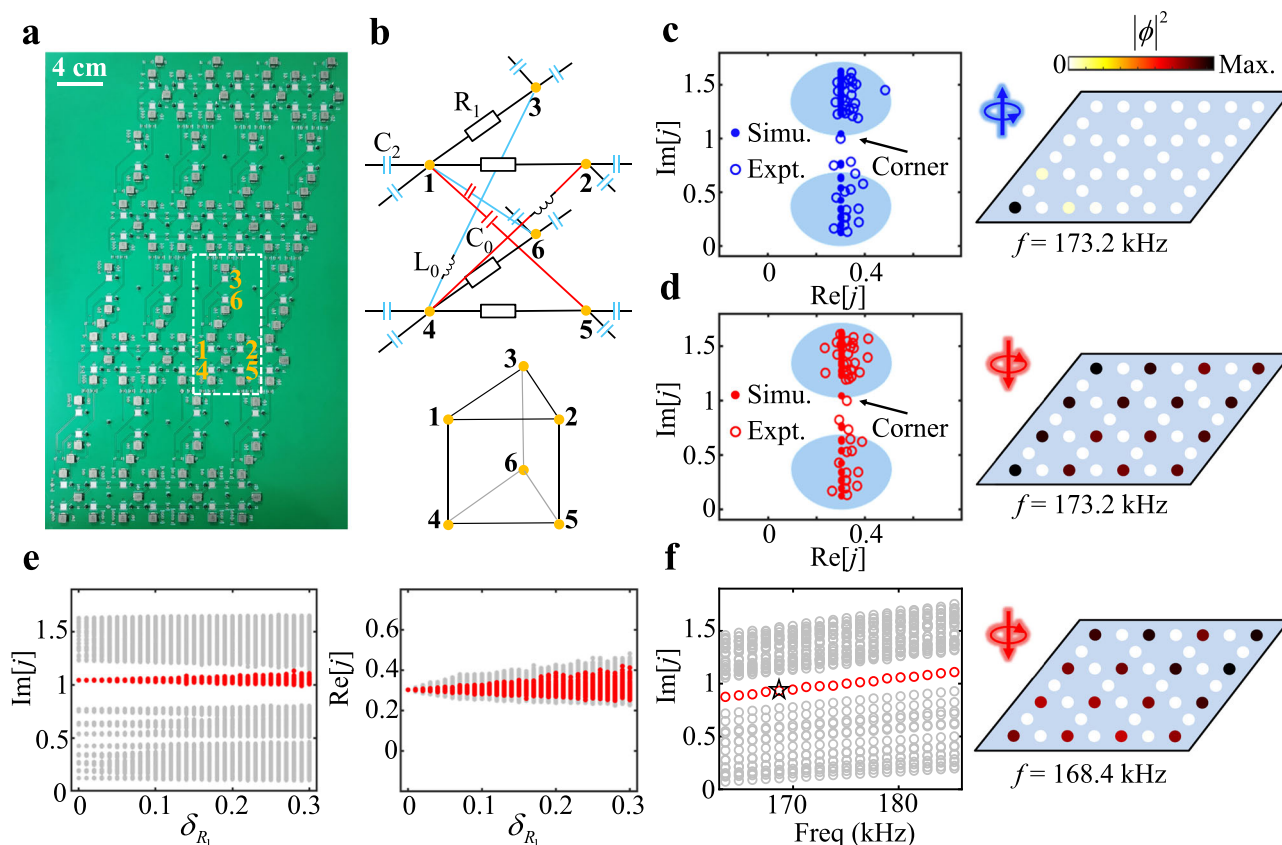
Fig. 4 | Observation of the second-order delocalization effect via loss.
a Photograph of the 2D passive circuit sample. **b** Schematic diagram of the designed circuit unit cell for the dashed rectangle in (**a**). The nodes 1–6 are correspond to the sublattices in 2D lattice. The intracell resistance R_1 and intercell capacitance C_2 are connected between nodes. The interlayer inductance L_0 and capacitance C_0 are connected along two directions. The circuit elements grounded at each node are introduced in Supplementary Section 6 to simplify the schematic. The bottom part shows the corresponding schematic of a lattice unit cell. **c**, **d** Simulated and measured OBC spectra for two spins. The blue backgrounds

denote the PBC spectra in theory. The corresponding measured eigenstate intensities of the TCMs are plotted on the right. The TCM of spin down is delocalized and forms the TDM. **e** Calculated OBC imaginary part of spectrum as a function of the resistance disorder δ_{R_1}. The corresponding eigenvalue's real part of the corner mode is shown on the right. **f** Measured OBC imaginary spectrum of spin down in a certain frequency range. The intensity of the marked eigenstate is shown on the right. The red and gray points in (**e**, **f**) indicate the eigenvalues of corner and other modes, respectively.

The second-order delocalization of TCM is visualized by utilizing a 2D passive electric circuit, as shown in Fig. 4a, which is designed on the bilayer kagome topological lattice. The corresponding circuit unit cell is schematically shown in Fig. 4b, where the circuit elements connected in m and n directions are the same with the 1D circuit. Again, the circuit Laplacian related with $H_2(\mathbf{k})$ can be similarly derived at a given frequency (Supplementary Section 6). Figure 4c, d show the measured OBC spectra of Laplacian for two spins at $f = 173.2$ kHz, respectively, where the blue backgrounds indicate the PBC spectra calculated in theory, separating two bulk bands. As observed, the measured TCMs are still in the gap. The measured eigenstate intensities of TCMs are shown in the right side of Fig. 4c, d, respectively, indicating the shape change of their wavefunctions. Owing to the passive bilayer structure combines pseudospin degree of freedom and loss, the originally localized TCM is more bound in the left-lower corner for spin up, and is delocalized forming a nearly flat TDM for spin down. The intensities of bulk and edge wavefunctions are also experimentally observed in Fig. S8 of Supplementary Section 6, which both exhibit the corner NHSEs.

To verify the topological feature of loss induced TDM, we provide the OBC real and imaginary spectra in the presence of resistance disorder. The resistance is changed to $R_1\left(1 + w\delta_{R_1}\right)$ with the disorder strength of δ_{R_1}, where w is a random number uniformly distributed from -1 to 1. We calculate 50 times for each δ_{R_1}. The calculated results shown in Fig. 4e prove that the TDM is still embedded in the imaginary band gap, robust against such disorders. Meanwhile, the loss induced

TDM is also robust against defects, as discussed in Supplementary Section 7. In particular, we show the measured imaginary spectra in a broad frequency range in Fig. 4f. Although the condition of forming a TDM needs a fixed frequency f_0 to keep the interlayer hoppings equal, the TCMs are still well delocalized in a certain frequency range. The intensity distribution of eigenstate at $f = 168.4$ kHz shown in the right panel of Fig. 4f is a concrete example to reveal the broadband property of TDM. These results denote the advantage of loss in inducing TBMs' delocalization.

Third-order TDM delocalized from TCM through loss in 3D

In 3D case, a bilayer pyrochlore lattice with deliberately introduced loss is proposed and shown in Fig. 5a, where the unit cell contains four sites 1–4 in each layer, and the hoppings in m, n and l directions are the same with the 1D chain. The two independent spin models can also be derived via the unitary transformation from the Hamiltonian $H_3(\mathbf{k})$ (Supplementary Section 8). The Hamiltonian of spin down model can be expressed as

$$H_{3\downarrow} = \begin{pmatrix} 0 & i(\gamma - t_0) + h_{12} & i(\gamma - t_0) + h_{13} & i(\gamma - t_0) + h_{14} \\ i(\gamma + t_0) + h_{12}^* & 0 & h_{23} & h_{24} \\ i(\gamma + t_0) + h_{13}^* & h_{23}^* & 0 & h_{34} \\ i(\gamma + t_0) + h_{14}^* & h_{24}^* & h_{34}^* & 0 \end{pmatrix},$$
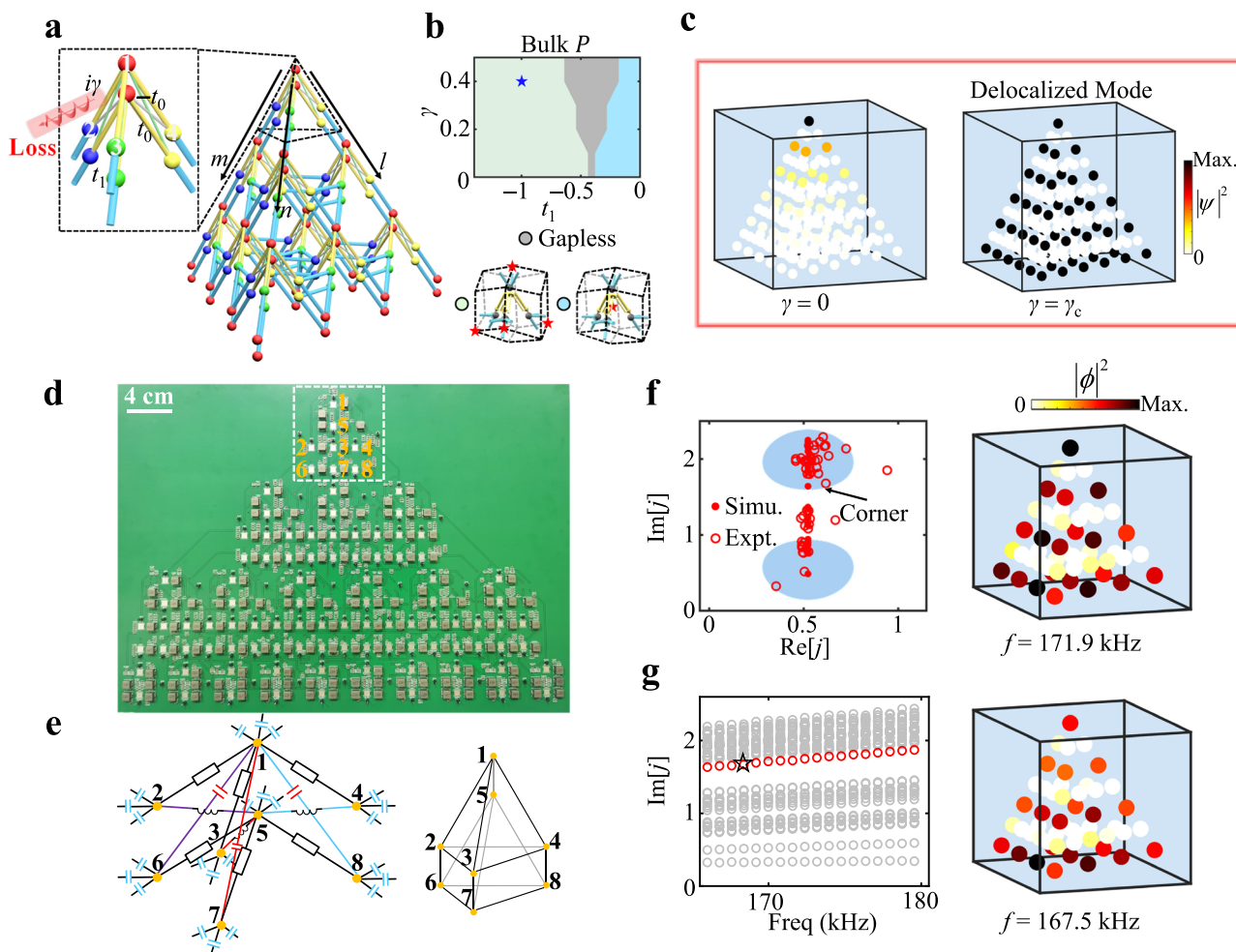
$$(4)$$

Fig. 5 | Demonstration of the third-order delocalization effect through loss in 3D. a Schematic of the 3D bilayer pyrochlore lattice. The red, blue, green and yellow balls represent different sublattices, where the different hoppings are indicated by the same colors as those in the 1D case. **b** Topological phase diagram of spin down model with $t_0 = 0.6$. It is also the same for spin up. The blue star marks the parameters of TDM, as $t_0 = 0.6$, $t_1 = -1$ with $\gamma_c = 0.4$. The red stars indicate the location of Wannier centers. **c** Wavefunction intensities of TCMs at different parameters for spin down, respectively. The bilayer pyrochlore lattice has 322 sites. **d** Photograph of the 3D passive circuit sample, which is designed on the 2D plane. **e** Schematic diagram of the designed circuit unit cell for the dashed rectangle in (**d**). The nodes 1–8 are correspond to the sublattices in 3D lattice. The intracell resistance R_1, intercell capacitance C_2, interlayer inductance L_0 and interlayer capacitance C_0 are connected along three directions, respectively. The circuit elements grounded at each node are described in Supplementary Section 9. **f** Simulated and measured OBC spectra for spin down. The blue backgrounds denote the PBC spectra in theory. The corresponding measured eigenstate intensity of the TDM is plotted on the right. **g** Measured OBC imaginary spectrum of spin down in a certain frequency range. The red and gray circles indicate the eigenvalues of corner and other modes, respectively. The intensity of the marked TCM is shown on the right.

where $h_{12} = t_1 e^{-i(k_x + k_y)/2}$, $h_{13} = t_1 e^{-i(k_y + k_z)/2}$, $h_{14} = t_1 e^{-i(k_x + k_z)/2}$, $h_{23} = t_1 e^{-i(k_z - k_x)/2}$, $h_{24} = t_1 e^{-i(k_z - k_y)/2}$ and $h_{34} = t_1 e^{-i(k_x - k_y)/2}$. The bottom sites of the OBC bilayer lattice are cut off, leaving only TCMs at top corners for two spins. By similarly employing the OBC real-space eigen-equations for spin down, the TCM's wavefunction decay ratio at top corner sublattice site A can be derived as $\epsilon_{A,\downarrow} = -i\frac{\gamma + t_0}{t_1}$, which is the same in m, n and l directions. Therefore, the critical parameter $\gamma = \gamma_c$ with $|\epsilon_{A,\downarrow}| = 1$ leads to a third-order delocalization of the TCM for forming a delocalized mode. The TDM is still topologically nontrivial, which is characterized by the non-Hermitian bulk polarization, as shown in Fig. 5b (Supplementary Section 8). The nontrivial phase (green) and trivial phase (blue) indicate the Wannier centers (red stars) located at the centers of the downward-pointing and upward-pointing tetrahedrons, respectively. Consequently, the originally localized third-order TCM can be fully delocalized in the whole 3D spin down lattice via loss, as shown in Fig. 5c.

The third-order delocalization of TCM is achieved by employing a 3D passive electric circuit, as shown in Fig. 5d. Owing to the reciprocal

loss modulation necessitates only passive and simple components, the 3D passive electric circuit based on the bilayer pyrochlore lattice is easily designed on the 2D plane (Supplementary Section 9). Figure 5e schematically depicts the circuit unit cell, where the same circuit elements as those in the 1D circuit are employed in m, n and l directions. The corresponding measured OBC eigenvalues and eigenstate intensity of Laplacian for spin down are shown in Fig. 5f at $f = 171.9$ kHz. Consistent with theoretical predictions, the eigenvalue of TCM remains in the gap, while its wavefunction shows remarkable delocalization, giving rise to the TDM. The intensity of the topological bound mode for spin up is also experimentally observed (Supplementary Section 9). This TDM also possesses broadband property, as demonstrated in Fig. 5g. The intensity distribution of eigenstate at $f = 167.5$ kHz indicates that the TDM is almost uniformly distributed even it deviates from the required frequency. Meanwhile, the topological properties of the TDMs remain unaffected across different dimensions within a certain frequency range (Supplementary Section 10). These excellent results in 1D, 2D and 3D all demonstrate that

the proposed passive system with loss always maintains stability, featuring a simple design and compact size, regardless of both the number of sites and system dimensions, paving the way for high-dimensional or other systems.

Discussion

In summary, we have realized the delocalization of the originally localized TBMs via only loss, which still preserve the nontrivial topological properties. In contrast to the conventional cognition of loss with localization, we here realize the delocalization, thereby broadening the understanding of loss. The proposed bilayer theoretical models integrating pseudospin degree of freedom with non-Hermitian loss are inherently built on reciprocal systems and fundamentally differ from the models in previous studies on non-reciprocal systems. Compared with the complicated non-reciprocal approaches, our work presents a distinct reciprocal paradigm in both theoretical framework and experimental design, which can be more readily generalized to explore and validate non-Hermitian topological phenomena in high-dimensional or other systems. The loss induced acoustic TDM has also been realized to demonstrate the universality of our work (Supplementary Section 11). Owing to the delocalized feature, these TDMs have potential applications, such as large-area single mode topological amplifier and high-performance energy harvesting in gap. We take the large-area single mode topological amplifier as an example and discussed it in Supplementary Section 12.

Methods

Mapping between the eigenstates of the Laplacian J and the voltage distribution

For a given frequency $\omega = 2\pi f$, the canonical form of Laplacian is given by

$$J(\omega) = P\Lambda P^{-1} = \sum_{n=1}^{N} j_n \boldsymbol{\phi}_n^R \boldsymbol{\phi}_n^L,$$

where $P = \left[\boldsymbol{\phi}_1^R, \boldsymbol{\phi}_2^R, \cdots, \boldsymbol{\phi}_N^R\right]$, $\Lambda = \mathrm{diag}(j_1, j_2, \cdots, j_N)$, $P^{-1} = \left[\boldsymbol{\phi}_1^L; \boldsymbol{\phi}_2^L; \cdots; \boldsymbol{\phi}_N^L\right]$, and j_n, $\boldsymbol{\phi}_n^R$ and $\boldsymbol{\phi}_n^L$ are the eigenvalue, right and left eigenstate of $J(\omega)$, respectively. The Green's function is obtained as

$$G(\omega) = J^{-1}(\omega) = P\Lambda^{-1}P^{-1} = \sum_{n=1}^{N} \frac{\boldsymbol{\phi}_n^R \boldsymbol{\phi}_n^L}{j_n}.$$

As a result, we can describe the voltage distribution of the circuit system to the input current via $\boldsymbol{V} = \sum_{n=1}^{N} \frac{\boldsymbol{\phi}_n^R \boldsymbol{\phi}_n^L}{j_n} \boldsymbol{I}$, which indicates the mapping between the eigenstates and voltage distribution[20,34]. Therefore, for an input current at one or several nodes with frequency ω, the corresponding voltage response is the combination of the eigenstates and the input current.

Assumptions in the theoretical model and the uncertainties in experimental measurements

It needs to be mentioned that, the equal positive and negative interlayer hoppings require $f = \frac{1}{2\pi\sqrt{L_0 C_0}}$ as the critical frequency f_0 to make sure this. Meanwhile, we connect certain grounding capacitances to different nodes to ensure that their respective on-site potentials of circuit Laplacian are equal. However, when the frequency deviates from the critical one, the on-site potential of each node is no longer strictly equal. At this time, it is not rigorous to transform the Laplacian into two spins via the unitary transformation. Therefore, in this paper, we primarily discuss the TDM of the spin Laplacians at the critical frequency. For the frequency variation near f_0, the Laplacian operator is approximately regarded as being capable of being transformed into two spins. The experimental results exhibit that the TDM can remain

uniform in a certain frequency near f_0, which so called the broadband property. In addition, we have thoroughly discussed the uncertainties in experimental measurements, which can be found in Supplementary Section 13.

Sample fabrications and experimental measurements

The specific values of the circuit elements used for the passive non-Hermitian circuits are chosen with manufacturing tolerances as $C_0 = 220$ nF($\pm 5\%$), $C_1 = 68$ nF($\pm 5\%$), $C_2 = 369$ nF($\pm 5\%$), $L_0 = 4.4$ uH ($\pm 10\%$) and $R_1 = 6.65\,\Omega(\pm 0.1\%)$. The 1D, 2D and 3D OBC circuits include 26 nodes, 80 nodes and 100 nodes, respectively. In the 2D and 3D samples, we take the same values for the circuit elements to the 1D one. The experimental measurements for the eigenvalues and eigenstates of circuit Laplacian are performed by measuring the impedance matrix $G_{ab} = V_a/I_b$. When we set a local input current I_b at node b, the voltage response V_a against ground at any node a is measured. The complete matrix G is the inverse of the circuit Laplacian J, which contains the full information of system, including eigenvalues and eigenstates of admittance. The 1D electric circuit shown in Fig. 2a possesses two three-port switches, where the circuit can be switched to PBC by connecting left end and right end; or switched to OBC by connecting the left end to the ground and the right end to the remaining two sites. Specifically, for the measurement of PBC, we place the input current on each node of a single unit cell in turn and measure the corresponding voltage responses of all the circuit nodes. By employing the Fourier transform, the Laplacian in the momentum space can be obtained. To measure the Laplacian of OBC, we place the input current on each node of the whole circuit in turn and measure the corresponding voltage response of all nodes. The measured Laplacian of spin model is obtained by the unitary transformation of the measured Laplacian $J' = TJT^{-1}$. The Keysight E5061B ENA vector network analyzer is employed to perform the measurements, where the input current is generated from the voltage source injected into each node through a resistance. It needs to be mentioned that, the theoretical frequency of forming a flat TDM is $f_0 = 161.8$ kHz due to the requirement of equal interlayer hoppings, the best TDMs formed in experiments are at 178 kHz, 173.2 kHz and 171.9 kHz for 1D, 2D and 3D samples, respectively. It is mainly owing to the actual values of the circuit components have certain deviations compared with the nominal values, which can be improved by screening circuit elements with smaller errors.

Data availability

All the data supporting this study are displayed in the main text and Supplementary Information. All data related to this study are available from the corresponding authors upon request.

Code availability

The codes that support the results of this study are available from the corresponding authors upon request.

References

1. Kosterlitz, J. M. Nobel lecture: topological defects and phase transitions. *Rev. Mod. Phys.* **89**, 040501 (2017).
2. Bansil, A., Lin, H. & Das, T. Colloquium: topological band theory. *Rev. Mod. Phys.* **88**, 021004 (2016).
3. Hatsugai, Y. Chern number and edge states in the integer quantum hall-effect. *Phys. Rev. Lett.* **71**, 3697–3700 (1993).
4. Wang, J. & Zhang, S. C. Topological states of condensed matter. *Nat. Mater.* **16**, 1062–1067 (2017).
5. Paulose, J., Chen, B. G. G. & Vitelli, V. Topological modes bound to dislocations in mechanical metamaterials. *Nat. Phys.* **11**, 153–156 (2015).
6. Hafezi, M., Demler, E. A., Lukin, M. D. & Taylor, J. M. Robust optical delay lines with topological protection. *Nat. Phys.* **7**, 907–912 (2011).

7. He, H. L. et al. Topological negative refraction of surface acoustic waves in a Weyl phononic crystal. *Nature* **560**, 61–64 (2018).

8. Barik, S. et al. A topological quantum optics interface. *Science* **359**, 666–668 (2018).

9. Mittal, S., Goldschmidt, E. A. & Hafezi, M. A topological source of quantum light. *Nature* **561**, 502–506 (2018).

10. Lu, J. Y. et al. Observation of topological valley transport of sound in sonic crystals. *Nat. Phys.* **13**, 369–374 (2017).

11. Wang, J. Q. et al. Extended topological valley-locked surface acoustic waves. *Nat. Commun.* **13**, 1324 (2022).

12. Mitchell, N. P., Nash, L. M., Hexner, D., Turner, A. M. & Irvine, W. T. M. Amorphous topological insulators constructed from random point sets. *Nat. Phys.* **14**, 380–385 (2018).

13. Albert, V. V., Glazman, L. I. & Jiang, L. Topological Properties of Linear Circuit Lattices. *Phys. Rev. Lett.* **114**, 173902 (2015).

14. Imhof, S. et al. Topolectrical-circuit realization of topological corner modes. *Nat. Phys.* **14**, 925–929 (2018).

15. Li, Y. H., Liang, C., Wang, C. Y., Lu, C. C. & Liu, Y. C. Gain-Loss-Induced Hybrid Skin-Topological Effect. *Phys. Rev. Lett.* **128**, 223903 (2022).

16. Lee, T. E. Anomalous Edge State in a Non-Hermitian Lattice. *Phys. Rev. Lett.* **116**, 133903 (2016).

17. Kawabata, K., Shiozaki, K. & Ueda, M. Anomalous helical edge states in a non-Hermitian Chern insulator. *Phys. Rev. B* **98**, 165148 (2018).

18. Alvarez, V. M. M., Vargas, J. E. B. & Torres, L. E. F. F. Non-Hermitian robust edge states in one dimension: Anomalous localization and eigenspace condensation at exceptional points. *Phys. Rev. B* **97**, 121401 (2018).

19. Liu, G. G. et al. Localization of Chiral Edge States by the Non-Hermitian Skin Effect. *Phys. Rev. Lett.* **132**, 113802 (2024).

20. Zou, D. Y. et al. Observation of hybrid higher-order skin-topological effect in non-Hermitian topolectrical circuits. *Nat. Commun.* **12**, 7201 (2021).

21. Lee, C. H., Li, L. H. & Gong, J. B. Hybrid higher-order skin-topological modes in nonreciprocal systems. *Phys. Rev. Lett.* **123**, 016805 (2019).

22. Zhu, W. W., Teo, W. X., Li, L. H. & Gong, J. B. Delocalization of topological edge states. *Phys. Rev. B* **103**, 195414 (2021).

23. Cheng, W. J., Zhang, X. J., Lu, M. H. & Chen, Y. F. Competition between band topology and non-Hermiticity. *Phys. Rev. B* **105**, 094103 (2022).

24. Wang, W., Wang, X. L. & Ma, G. C. Non-Hermitian morphing of topological modes. *Nature* **608**, 50–55 (2022).

25. Wang, W., Wang, X. L. & Ma, G. C. Extended state in a localized continuum. *Phys. Rev. Lett.* **129**, 264301 (2022).

26. Wang, X. L., Wang, W. & Ma, G. C. Extended topological mode in a one-dimensional non-Hermitian acoustic crystal. *AAPPS Bull.* **33**, 23 (2023).

27. Lu, Z. Y. et al. Extended states isolated in the band gap in non-Hermitian electrical circuits. *Phys. Rev. Appl.* **21**, 034043 (2024).

28. Liu, C. et al. Extended state reshaping in non-Hermitian topolectrical circuits. *Phys. Rev. Appl.* **21**, 054013 (2024).

29. Fritzsche, A. et al. Parity-time-symmetric photonic topological insulator. *Nat. Mater.* **23**, 377–382 (2024).

30. Hu, B. L. et al. Non-Hermitian topological whispering gallery. *Nature* **597**, 655–659 (2021).

31. Yao, S. Y. & Wang, Z. Edge states and topological invariants of non-hermitian systems. *Phys. Rev. Lett.* **121**, 086803 (2018).

32. Weidemann, S. et al. Topological funneling of light. *Science* **368**, 311–314 (2020).

33. Zhang, L. et al. Acoustic non-Hermitian skin effect from twisted winding topology. *Nat. Commun.* **12**, 6297 (2021).

34. Helbig, T. et al. Generalized bulk-boundary correspondence in non-Hermitian topolectrical circuits. *Nat. Phys.* **16**, 747–750 (2020).

35. Gao, H. et al. Observation of topological edge states induced solely by non-Hermiticity in an acoustic crystal. *Phys. Rev. B* **101**, 180303 (2020).

36. Gu, Z. M. et al. Observation of an acoustic non-Hermitian topological Anderson insulator. *Sci. China Phys. Mech. Astron.* **66**, 294311 (2023).

37. Gao, H. et al. Non-Hermitian route to higher-order topology in an acoustic crystal. *Nat. Commun.* **12**, 1888 (2021).

38. Li, Y. H., Lu, C. C., Zhang, S. & Liu, Y. C. Loss-induced Floquet non-Hermitian skin effect. *Phys. Rev. B* **108**, 220301 (2023).

39. Zhang, X. J., Tian, Y., Jiang, J. H., Lu, M. H. & Chen, Y. F. Observation of higher-order non-Hermitian skin effect. *Nat. Commun.* **12**, 5377 (2021).

40. Zhang, K., Yang, Z. S. & Fang, C. Universal non-Hermitian skin effect in two and higher dimensions. *Nat. Commun.* **13**, 2496 (2022).

41. Zhou, Q. Y. et al. Observation of geometry-dependent skin effect in non-Hermitian phononic crystals with exceptional points. *Nat. Commun.* **14**, 4569 (2023).

42. Wang, W., Hu, M. Y., Wang, X. L., Ma, G. C. & Ding, K. Experimental realization of geometry-dependent skin effect in a reciprocal two-dimensional lattice. *Phys. Rev. Lett.* **131**, 207201 (2023).

43. Wu, J. et al. Spin-dependent localization of helical edge states in a non-hermitian phononic crystal. *Phys. Rev. Lett.* **133**, 126601 (2024).

44. Yin, C. H., Jiang, H., Li, L. H., Lü, R. & Chen, S. Geometrical meaning of winding number and its characterization of topological phases in one-dimensional chiral non-Hermitian systems. *Phys. Rev. A* **97**, 052115 (2018).

45. Aquino, R., Lopes, N. & Barci, D. G. Critical and noncritical non-Hermitian topological phase transitions in one-dimensional chains. *Phys. Rev. B* **107**, 035424 (2023).

46. Song, F., Yao, S. Y. & Wang, Z. Non-hermitian topological invariants in real space. *Phys. Rev. Lett.* **123**, 246801 (2019).

47. Longhi, S. Probing non-Hermitian skin effect and non-Bloch phase transitions. *Phys. Rev. Res.* **1**, 023013 (2019).

48. Yang, Z. H., Zhou, K. L., Zeng, B. W. & Hu, Y. Inverse design of winding tuple for non-Hermitian topological edge modes. *Phys. Rev. B* **111**, L041406 (2025).

49. Zhang, X. W. et al. Observation of continuum Landau modes in non-Hermitian electric circuits. *Nat. Commun.* **15**, 1798 (2024).

50. Zhu, P. H., Sun, X. Q., Hughes, T. L. & Bahl, G. Higher rank chirality and non-Hermitian skin effect in a topolectrical circuit. *Nat. Commun.* **14**, 720 (2023).

51. Rafi-Ul-Islam, S. M., Bin Siu, Z., Razo, M. S., & Jalil, M. B. Frequency-controlled critical non-Hermitian skin effect in a topolectrical circuit. *Phys. Rev. B* **112**, 045402 (2025).

52. Wang, H. F., Xie, B. Y. & Ren, W. Finite-size-induced non-Hermitian phase transitions in real space. *Sci. China-Phys. Mech. Astron.* **67**, 117011 (2024).

53. Guo, C. X. et al. Scale-tailored localization and its observation in non-Hermitian electrical circuits. *Nat. Commun.* **15**, 9120 (2024).

54. Qian, L., Zhang, W. X., Sun, H. J. & Zhang, X. D. Non-Abelian topological bound states in the continuum. *Phys. Rev. Lett.* **132**, 046601 (2024).

55. Kim, Y. et al. Realization of non-Hermitian Hopf bundle matter. *Commun. Phys.* **6**, 273 (2023).

56. Wang, H. F., Xie, B. Y. & Ren, W. Non-Hermitian reconstruction of photonic hierarchical topological states. *Commun. Phys.* **6**, 347 (2023).

Acknowledgements

Author contributions

Competing interests

The authors declare no competing interests.

Additional information

Supplementary information The online version contains supplementary material available at https://doi.org/10.1038/s41467-025-65422-7.

Correspondence and requests for materials should be addressed to Weiyin Deng, Hua Cheng, Zhengyou Liu or Shuqi Chen.

Peer review information *Nature Communications* thanks the anonymous reviewer(s) for their contribution to the peer review of this work. A peer review file is available.

Reprints and permissions information is available at http://www.nature.com/reprints

Publisher's note Springer Nature remains neutral with regard to jurisdictional claims in published maps and institutional affiliations.